IEEE Access
Multidisciplinary | Rapid Review | Open Access Journal

Received December 20, 2021, accepted January 4, 2022, date of publication January 12, 2022, date of current version January 20, 2022.

Digital Object Identifier 10.1109/ACCESS.2022.3142521

Research on the Turning Maneuverability of a Bionic Robotic Dolphin

ZHONGHUA YANG, WEIJIE GONG, HONG CHEN, SEN WANG, AND GUOJING ZHANG
College of Mechatronics and Control Engineer, Shenzhen University, Shenzhen 515061, China
Corresponding author: Weijie Gong (gongwj@szu.edu.cn)

ABSTRACT This paper studies four patterns for the maneuverability of robotic dolphins: turning with flapping flippers, turning with swing flippers, turning with head offset, and turning with head-flipper coordination. Turning maneuverability is one of the important evaluation indexes for the performance of underwater bionic robots, and existing literature has rarely theoretically or experimentally evaluated turning maneuverability for the latter two turning patterns. In this paper, we establish a dynamic model for the high maneuverability of underwater bionic robots and discuss the influence of motion design parameters, including the frequency of the pectoral fins and the offset angle of the head, on the turning maneuverability, focusing on the turning angular velocity and turning radius. To verify the effectiveness and control accuracy of the dynamic model, we develop a multidegree-of-freedom (multi-DOF) and high-maneuverability bionic robotic dolphin and test its maneuverability through experiments. Extensive experimental results demonstrate that the established dynamic model can successfully predict the turning maneuverability of robotic dolphins. In addition, the turning methods in this paper have better turning performance than some robotic fish. This paper provides a reference for the establishment of a maneuvering dynamics model for underwater bionic robots and a theoretical basis for the design of a turning maneuver control system.

INDEX TERMS Robotic dolphin, dynamic model, turning pattern, maneuverability.

I. INTRODUCTION

In recent decades, various autonomous underwater vehicles (AUVs) have been used to explore marine resources. Traditional AUVs are propelled using rotatory propellers, which have low propulsion efficiency and high noise. However, aquatic species such as fish or cetaceans have undergone tens of millions of years of evolution, developing extraordinary swimming performance, including maneuverability, stability, and rapidity. As a result, an increasing number of researchers have become interested in developing biologically inspired robotic fish [1]–[5]. These include servo/IPMC-driven robotic fish [6], single-jointed biomimetic box fish [7], amphibious robotic fish [8], and gliding robotic dolphins [9]. Robotic fish have great potential application value in marine pipeline exploration, underwater detection, and water quality environmental monitoring due to their high maneuverability performance [10], [11].

As a critical factor in designing robotic fish and exploring their maneuverability, a dynamic model has been studied by many scholars in the early years. Taylor's resistive theory [12] is simple but loses sight of the role of inertial forces and can only apply to a case with a low Reynolds number. Lighthill's elongated body theory [13], which takes the influence of the added mass effect into consideration, can maintain a good balance between fidelity and simplicity and is chiefly used in the modeling of slender robotic fish. Tong's waving plate theory [14] approaches the dynamic modeling of robotic fish with fewer joints. Quasi-steady hydrofoil theory [15], both simple and efficient, is suitable for the study of most robotic fish. As computational fluid dynamics develops, the hydrodynamic parameters of robotic fish can also be obtained by solving the Navier-Stokes equations [16]. This approach is of high precision, but it takes a long time to calculate. However, the dynamic model established using AUVs is relatively simple, which only analyzes the overall force on the underwater vehicles, including the gravity, buoyancy, propeller propulsion and hydrodynamic force of the vehicle.

To hunt and avoid predators, the fish in the ocean have to have high mobility. For example, muskellunge can quickly turn at a maximum angular velocity of 2500 °/s [17]. Inspired by the turning mobility of fish, scientists and engineers

The associate editor coordinating the review of this manuscript and approving it for publication was Shuhuan Wen.

have been interested in the turning motion of robotic fish [5], [18], [19]. Liu *et al.* developed a bionic robotic dolphin mainly made up of a pair of single-joint pectoral fins and a double-joint caudal fin, which employs the turning pattern of a median and/or paired fin (MPF) [20]. This method analyzes the turning radius but overlooks the influence of the turning speed on turning performance. Tan *et al.* conducted a study of the turning performance of single-joint robotic fish [21]. As shown in the experimental and simulation results, only the offset angle of the caudal fin impacts the turning radius, and this turning pattern can only optimize the turn performance limitedly. Li *et al.* developed a yaw control method for the steering motion of robotic fish, which is based on a balanced learning algorithm [22]. Turning a circle takes 300 s and the turning radius is 2.5 m. Although this method can be used to carry out autonomous control, it has a long turning time and a large turning radius, which goes against practical applications. Chen *et al.* designed a microrobotic fish with a body 89 mm in length, in which an electromagnetic driver is used to articulate the single-joint tail fin left and right [23]. A turning radius of 183.14 mm can be achieved at 2.87 Hz. Although the turning radius is numerically smaller, it is still 2.06 times as long as the body. In the above studies, the offset turning pattern of the caudal fin is mostly used in robotic fish, while the MPF turning pattern is in robotic dolphins. A single turning pattern cannot be well applied to a variety of occasions required in mobility. Moreover, some have a larger turning radius and longer turning time, and others are limited in their degree of optimizing the turning maneuverability.

Therefore, this paper raises maneuverability research on multiple turning patterns in connection with the problems existing in previous studies on the turning performance of robotic fish and robotic dolphins. The specific research content and contributions are as follows.

1) Developed a robotic dolphin with high maneuverability. Turning maneuverability is one of the important evaluation indexes of underwater bionic robots. For existing bionic robotic dolphins, due to the up and down motion of the caudal fin that provides the main propulsion force, a yaw moment cannot be generated. We can only rely on pectoral fins for turning, resulting in a poor turning performance. Therefore, we developed a robotic dolphin with a yaw joint in the head and carried out underwater tests, indicating that the turning performance is greatly improved because of the cooperative movement of the head yaw joint and pectoral fins.

2) Maneuvering dynamics model. A dynamic model based on quasi-steady hydrofoil theory and the Newton-Euler equation of a multi-DOF robotic dolphin with high maneuverability is established, which can provide a theoretical basis for the establishment of similar multijoint underwater bionic robots. In particular, the correctness and effectiveness of the dynamic model are verified through experiments based on a high-precision motion capture camera.

3) Four typical turning patterns. We propose four turning patterns for the robotic dolphin, including a flapping-wing turning pattern, swinging-wing turning pattern, head-offset turning pattern, and pattern of cooperative turning using the head and flippers. Furthermore, the latter two turning patterns are rarely studied in other literature.

4) Research on turning maneuverability. We studied the relationship between motion parameters, including pectoral fin frequency and head offset angle, and turning performance based on the turning radius and turning angular velocity, which has certain guiding significance for the maneuverability control of underwater bionic robots. In addition, we have better turning performance than some other robotic fish.

The remainder of this paper is arranged as follows. Section II introduces the design and four turning patterns of the robotic dolphin prototype and Section III discusses the development of the robotic dolphin dynamic model. In Section IV, an analysis of the maneuverability of four turning patterns is performed through simulation and experiment. Section V provides the conclusion of the paper and the prospects of future work.

II. STRUCTURE OF A ROBOTIC DOLPHIN AND TURN MOTION ANALYSIS

A. DESIGN OF MECHANICAL STRUCTURE

A bottle-nosed dolphin has a streamlined body structure, which can reduce the resistance during swimming, and its soft and flexible body is mobile. From the perspective of mechanical engineering, the streamlined structure of a bionic robotic dolphin is easy to achieve, but its flexible body is difficult to simulate. Generally, it is replaced with a rigid body. To alleviate the shortage of mobility arising from an the inflexible body, a multijoint structure design is used herein.

The mechanical design of the robotic dolphin is shown in Fig. 1. A bottle-nosed dolphin is taken as the bionic object, and its streamlined body is imitated to reduce swimming resistance. Broadly speaking, the robotic dolphin is mainly composed of four parts: a two-DOF head, a pair of double-joint pectoral fins, a single-joint caudal fin, and a rigid body. Its head contains two servomotors vertically distributed to control the yaw motion and pitching motion of the robotic dolphin. The pectoral fins are symmetrically distributed with two servomotors to control the flapping-wing and swinging-wing motion. The caudal fin is designed with a crescent structure to increase thrust and swimming speed. To balance the torque in the roll direction and increase the driving force of the caudal fin, a transmission mechanism driven by double motors is used. The rigid body mainly contains batteries, several control boards, a barycenter regulating mechanism, and a double-motor transmission mechanism. The shell of the robotic dolphin is made of light-cured resin using 3D printing technology. Light-cured resin is high in curing degree and good in toughness with a certain compressive strength. In addition, it has less organic volatilization and is environmentally friendly. The main characteristics of the robotic dolphin are shown in Table 1.

TABLE 1. Technical specifications of the robotic dolphin.

Parameter	Characteristics
Size (L × W × H)	1.011 m × 0.255 m × 0.236 m
Total mass	15.020 kg
Joint distribution	Head: 2; Pectoral fins: 4; Caudal fin:1
Driver mode	Brushless DC motor, Digital servomotor
Control mode	Wireless
Power supply	Lithium battery (DC 24 V)

B. ANALYSIS OF THE TURNING PATTERN

Robotic fish can turn by generating yawing moments through the offset of the caudal fin or with the assistance of pectoral fins. The caudal fin cannot generate a robotic dolphin turning torque because it swings up and down. Such a dolphin can make a turn only by relying on a yawing torque from a phase differences in the swing of the left and right pectoral fins or from the swing of the unilateral pectoral fin. Its turning performance does not exceed that of robotic fish. Therefore, to improve the turning maneuverability of robotic dolphins, the robotic dolphin studied here contains a yawing joint in the head, which can work with flippers to make a turn.

Fig. 2 shows the four turning patterns of the robotic dolphin, which are designated the flapping-wing turning pattern, swinging-wing turning pattern, head-offset turning pattern, and head-flipper synergetic turning pattern. To facilitate the description, the four patterns are subsequently defined as Pattern I, Pattern II, Pattern III, and Pattern IV. Pattern I has the features of the swinging-wing joints not moving and the left and right pectoral fins conduct a front-and-back flapping motion with a phase difference. Pattern II is characterized by the immobility of the flapping-wing joints, the swinging-wing movement of the pectoral fins, and the differential motion of the left and right pectoral fins. Pattern III is characterized by the pectoral fin remaining stationary and the fin surface remaining parallel to the horizontal plane, with the head offset to the left or right at different angles to turn the robotic dolphin. Pattern IV combines the characteristics of the pectoral fin and head-turning patterns.

III. DYNAMIC MODELING OF THE ROBOTIC DOLPHIN

In this section, we adopt quasi-steady hydrofoil theory and the Newton-Euler equation as the main framework to establish the dynamic modeling of the robotic dolphin.

A. KINEMATIC ANALYSIS

The kinematics model is mainly used to describe the motion state of a robotic dolphin in space and the position and attitude of each joint.

To describe the movement of the robotic dolphin, the robot is simplified into a joint structure diagram, and a coordinate system is established, as shown in Fig. 3. We use $[X, Y, Z]^T$ to denote inertial coordinates, $[x_0, y_0, z_0]^T$ to denote a body coordinate system with the body centroid as the origin, and $[\boldsymbol{i}, \boldsymbol{j}, \boldsymbol{k}]^T$ to represent a unit vector. In the inertial coordinate system, the roll, yaw, and pitch of the robot are expressed as ψ, φ, and γ, respectively. The velocity of the robotic dolphin is denoted by $\boldsymbol{V}$, consisting of longitudinal velocity V_x, vertical velocity V_y, and lateral velocity V_z, and the

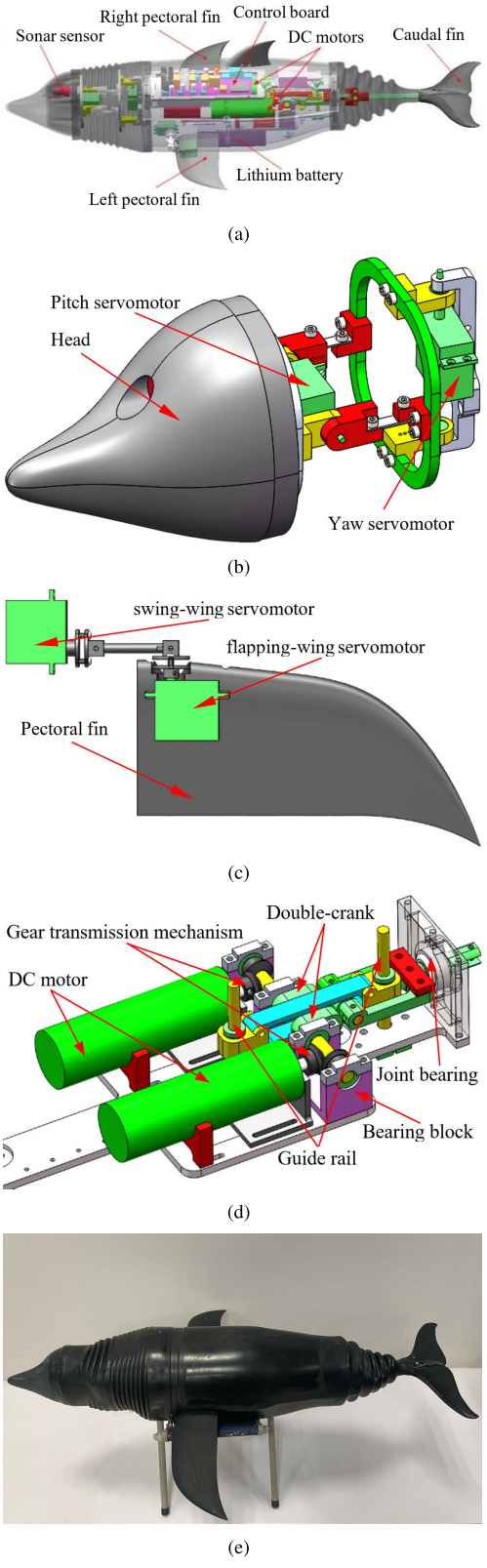

FIGURE 1. Mechanical design of the robotic dolphin. (a) Conceptual design. (b) Head mechanism. (c) Pectoral fin. (d) Motor driving device. (e) Robotic dolphin prototype.

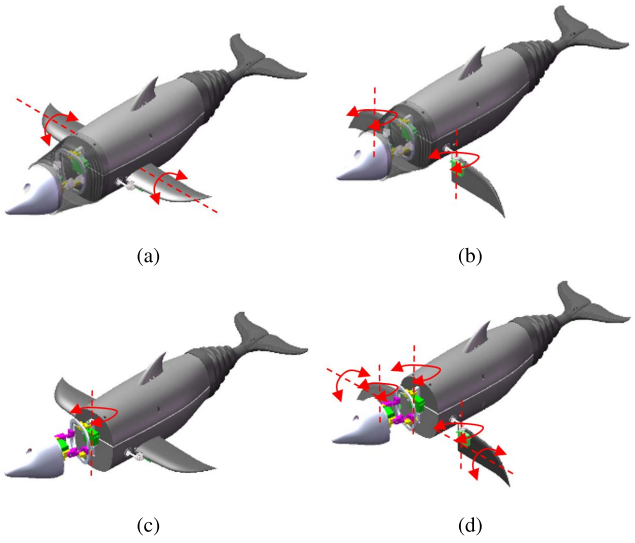

FIGURE 2. Four types of turning patterns. (a) Pattern I: flapping-wing turning pattern. (b) Pattern II: swing-wing turning pattern. (c) Pattern III: head-offset turning pattern. (d) Pattern IV: head-flippers coordination turning pattern.

angular velocity is defined as $\boldsymbol{\omega} = [\omega_x, \omega_y, \omega_z]^T$, expressed in the body coordinates. $[x_j, y_j, z_j]^T$ is the joint coordinate system, which is built using the Denavit-Hartenberg (D-H) Matrix [24]. Subscripts $j = 1, 2, 3, 4$, and 5 represent the caudal fin, the left swinging flipper, the left flapping flipper, the right swinging flipper, and the right flapping flipper of the robot, respectively.

The coordinate origin of each joint in the body coordinate system is positioned at $o_1 = (q_x, 0, 0)^T$, $o_{2,3} = (p_x, 0, -p_z)^T$, and $o_{4,5} = (p_x, 0, p_z)^T$. The centroid of the caudal fin in the caudal fin coordinate system is positioned at $C_1 = (-C_x, 0, 0)^T$. $C_2 = (0, r_y, -r_z)^T$ and $C_3 = (0, -r_y, -r_z)^T$ are the centroid coordinates of the left and right pectoral fins in $[x_3, y_3, z_3]^T$ and $[x_5, y_5, z_5]^T$, respectively. C_x is the distance from the centroid of the caudal fin to the origin of the caudal fin joint coordinate system, and r_y and r_z are the distances from the centroid of the pectoral fins to Axis y_3 (y_5) and Axis z_3 (z_5), respectively.

The kinematic velocities of the caudal fin and flippers of the robotic dolphin are calculated in the body coordinate system, and each fin velocity of the robotic dolphin can be expressed as:

$$\boldsymbol{V}_i = \boldsymbol{V} + \boldsymbol{\omega} \times \boldsymbol{r}_i + \boldsymbol{v}_0^i \tag{1}$$

where $\boldsymbol{r}_i$ represents the vector from the body center separately to the centroid of the caudal fin, the left pectoral fin, or the right pectoral fin, "$\times$" is the cross product of vectors, and $\boldsymbol{v}_0^i$ denotes the velocity vector of each fin centroid in the body coordinate system.

According to the transformation technique of the D-H coordinates [24], the matrix for the joint coordinate

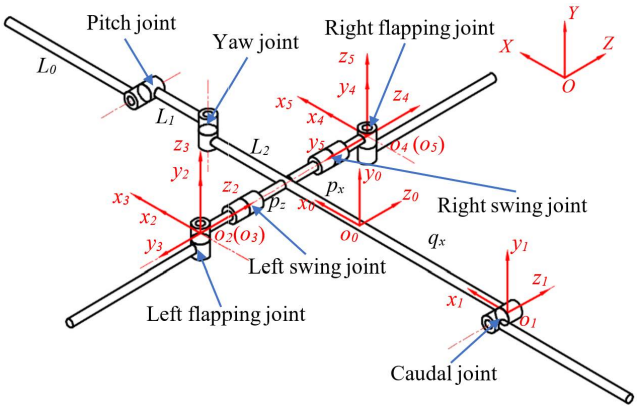

FIGURE 3. Coordinate systems including the inertial, body, and fin frames.

transformation is defined as follows:

$$\begin{aligned} {}^i_jT &= Rot(X, \alpha_i)Trans(X, a_i)Rot(Z, \theta_i)Trans(Z, d_i) \\ &= \begin{bmatrix} \cos\theta_i & -\sin\theta_i & 0 & \alpha_i \\ \sin\theta_i\cos\alpha_i & \cos\theta_i\cos\alpha_i & -\sin\alpha_i & -d_i\sin\alpha_i \\ \sin\theta_i\sin\alpha_i & \cos\theta_i\sin\alpha_i & \cos\alpha_i & d_i\cos\alpha_i \end{bmatrix} \end{aligned} \tag{2}$$

where α_i: $\{i\}$ rotates α_i around Axis X_i to make Axes Z_i and Z_j equidirectional; a_i: $\{i\}$ moves α_i along Axis X_i to make Axes Z_i and Z_j collinear; θ_i: $\{i\}$ rotates θ_i around Axis Z_i to make Axes Z_i and Z_j equidirectional; and d_i: $\{i\}$ moves d_i along Axis Z_i to make Axes Z_i and Z_j collinear.

The centroid of each fin in the body coordinate system is $\boldsymbol{r}_i = {}^j_0T[C_i; 1]$, where $j = 1, 3, 5$ and $i = 1, 2, 3$. The expressions of $\boldsymbol{r}_i$ and $\boldsymbol{v}_0^i$ follow that (3) and (4), as shown at the bottom of the next page, where θ_j and $\dot{\theta}_j$ are the rotation angle and the angular velocity of each joint, respectively, and $j = 1, 2, 3, 4, 5$.

B. FORCE ANALYSIS OF THE ROBOTIC DOLPHIN

To build the dynamic model of the robotic dolphin, we need to analyze the external forces it experiences. Such external forces mainly include the lift, drag, and fluid pressure caused by the caudal fin, the lift and drag caused by the pectoral fins, the resistance of the head and body, the gravity and buoyancy acting on the body, and the fluid inertia force.

1) FORCE ANALYSIS OF THE CAUDAL FIN

The caudal fin mainly experiences the influence of the trailing vortex on its lift and drag and the fluid pressure. Lift is defined as the force acting perpendicular to the direction of the motion and drag as the force acting parallel to and opposite to the direction of the motion. The direction of the fluid pressure is perpendicular to the surface of the caudal fin and opposite to its swing direction. From the high-aspect-ratio wing theory [25] and the quasi-steady hydrofoil theory [26],

the lift and resistance experienced by the caudal fin can be described as follows:

$$F'_{L1} = 2\pi\rho C_t L_t S_1 |V_1|^2 \sin\alpha_1 \tag{5}$$

$$F'_{D1} = \frac{1}{2}\rho C_{D1} |V_1|^2 S_1 \tag{6}$$

where ρ is the fluid density, C_t, L_t, S_1, and C_{D1} represent the chord length, elongation, surface area, and drag coefficient of the caudal fin, respectively, and α_1 is the angle of attack of the caudal fin, which is the angle included between the centerline of the caudal fin and the oncoming flow and can be expressed as:

$$\alpha_1 = \left|\frac{\pi}{2} - \langle \boldsymbol{n}_1, \boldsymbol{V}_1 \rangle\right| \tag{7}$$

where $\boldsymbol{n}_1$ is the vector normal to the caudal fin, which can be expressed as:

$$\boldsymbol{n}_1 = -\sin\theta_1 \boldsymbol{i} + \cos\theta_1 \boldsymbol{j} + 0\boldsymbol{k} \tag{8}$$

The drag coefficient of the caudal fin varies with the Reynolds number, as expressed by the empirical formula [27]:

$$C_{D1} = 15.4 \times Re^{-0.4} = 15.4 \times \left(\frac{l V_1}{\mu}\right)^{-0.4} \tag{9}$$

where μ is the coefficient of kinetic viscosity and l is the length of the caudal fin.

The drag expression for the caudal fin in the body coordinate system is:

$$\boldsymbol{F}_{D1} = -F'_{D1}\boldsymbol{n}_1 \tag{10}$$

Now that the lift is directionally perpendicular to the moving speed, there is:

$$\boldsymbol{k}_1 = \boldsymbol{n}_1 \times \boldsymbol{V}_1 \tag{11}$$

where $\boldsymbol{k}_1 = k_x\boldsymbol{i} + k_y\boldsymbol{j} + k_z\boldsymbol{k}$.

The rotation angle θ can be expressed as:

$$\theta = \begin{cases} \dfrac{\pi}{2}, & \cos\langle \boldsymbol{n}_1, \boldsymbol{V}_1 \rangle \geq 0 \\ -\dfrac{\pi}{2}, & \cos\langle \boldsymbol{n}_1, \boldsymbol{V}_1 \rangle < 0 \end{cases} \tag{12}$$

$$R_{k1} = \begin{bmatrix} k_x^2 v\theta + c\theta & k_{xy}v\theta - k_z s\theta & k_{xz}v\theta + k_y s\theta \\ k_{xy}v\theta + k_z s\theta & k_y^2 v\theta + c\theta & k_{yz}v\theta - k_x s\theta \\ k_{xz}v\theta - k_y s\theta & k_{yz}v\theta + k_x s\theta & k_z^2 v\theta + c\theta \end{bmatrix} \tag{13}$$

where k_{xy} represents $k_x k_y$, k_{xz} represents $k_x k_z$, k_{yz} represents $k_y k_z$, $v\theta$ is $1 - \cos\theta$, $c\theta$ is $\cos\theta$, and $s\theta$ is $\sin\theta$.

The lift acting on the robotic caudal fin is expressed in the body coordinates as:

$$\boldsymbol{F}_{L1} = R_{k1} F'_{L1} \widehat{\boldsymbol{V}}_1 \tag{14}$$

where $\widehat{\boldsymbol{V}}_1$ is the vector normal to $\boldsymbol{V}_1$.

We know from the Bernoulli principle that the fluid pressure acting on the caudal fin is calculated as [28]:

$$F'_p = \frac{1}{2}\rho |\boldsymbol{V}_1|^2 S_1 sgn(-\cos\langle \boldsymbol{n}_1, \boldsymbol{V}_1 \rangle) \tag{15}$$

Then, the expression of the fluid pressure in the body coordinate system is defined as follows:

$$\boldsymbol{F}_p = F'_p \boldsymbol{n}_1 \tag{16}$$

$$\begin{cases} \boldsymbol{r}_1 = \begin{bmatrix} -q_x - C_x\cos\theta_1 \\ -C_x\sin\theta_1 \\ 0 \end{bmatrix} \\ \boldsymbol{r}_2 = \begin{bmatrix} p_x - r_y\cos\theta_2\sin\theta_3 + r_z\sin\theta_2 \\ -r_y\sin\theta_2\sin\theta_3 - r_z\cos\theta_2 \\ -p_z - r_y\cos\theta_3 \end{bmatrix} \\ \boldsymbol{r}_3 = \begin{bmatrix} p_z + r_y\cos\theta_4\sin\theta_5 + r_z\sin\theta_4 \\ r_y\sin\theta_4\sin\theta_5 - r_z\cos\theta_4 \\ p_z + r_y\cos\theta_5 \end{bmatrix} \end{cases} \tag{3}$$

$$\begin{cases} \boldsymbol{v}_0^1 = \begin{bmatrix} C_x\dot{\theta}_1\sin\theta_1 \\ -C_x\dot{\theta}_1\cos\theta_1 \\ 0 \end{bmatrix} \\ \boldsymbol{v}_0^2 = \begin{bmatrix} r_y\dot{\theta}_2\sin\theta_2\sin\theta_3 - r_y\dot{\theta}_3\cos\theta_2\cos\theta_3 + r_z\dot{\theta}_2\cos\theta_2 \\ -r_y\dot{\theta}_2\cos\theta_2\sin\theta_3 - r_y\dot{\theta}_3\sin\theta_2\cos\theta_3 + r_z\dot{\theta}_2\sin\theta_2 \\ r_y\dot{\theta}_3\sin\theta_3 \end{bmatrix} \\ \boldsymbol{v}_0^3 = \begin{bmatrix} -r_y\dot{\theta}_4\sin\theta_4\sin\theta_5 + r_y\dot{\theta}_5\cos\theta_4\cos\theta_5 + r_z\dot{\theta}_4\cos\theta_4 \\ r_y\dot{\theta}_4\cos\theta_4\sin\theta_5 - r_y\dot{\theta}_5\sin\theta_4\cos\theta_5 + r_z\dot{\theta}_4\sin\theta_4 \\ -r_y\dot{\theta}_5\sin\theta_5 \end{bmatrix} \end{cases} \tag{4}$$

The moment acting on the caudal fin can be written as:

$$\boldsymbol{M}_1 = \boldsymbol{r}_1 \times (\boldsymbol{F}_{L1} + \boldsymbol{F}_{D1} + \boldsymbol{F}_p) \tag{17}$$

2) FORCE ANALYSIS OF THE PECTORAL FINS

The lift and drag mainly act on the pectoral fins in the fluid, and their directions are similar to those on the caudal fin, so the lift and drag acting on the left and right pectoral fins [26] are, respectively:

$$F'_{Li} = \frac{1}{2}\rho C_{Li} |\boldsymbol{V}_i|^2 S_i \tag{18}$$

$$F'_{Di} = \frac{1}{2}\rho C_{Di} |\boldsymbol{V}_i|^2 S_i \tag{19}$$

where C_{Li} represents the lift coefficient of a pectoral fin, C_{Di} represents its drag coefficient, S_i represents its surface area, and $i = 2, 3$.

For unsteady flow, the lift coefficient of the pectoral fins can be expressed as a function of the angle of attack [29]:

$$C_{Li} = 2\pi \sin\alpha_i \left(1 - 0.165e^{-0.0455\boldsymbol{V}_i t} - 0.335e^{-0.3\boldsymbol{V}_i t}\right) \tag{20}$$

$$\alpha_i = \left|\frac{\pi}{2} - \langle \boldsymbol{n}_i, \boldsymbol{V}_i \rangle\right| \tag{21}$$

where $\boldsymbol{n}_i$ is the vector normal to the pectoral fins, which can be expressed as:

$$\begin{cases} \boldsymbol{n}_2 = \cos\theta_2 \cos\theta_3 \boldsymbol{i} + \sin\theta_2 \cos\theta_3 \boldsymbol{j} - \sin\theta_3 \boldsymbol{k} \\ \boldsymbol{n}_3 = \cos\theta_4 \cos\theta_5 \boldsymbol{i} + \sin\theta_4 \cos\theta_5 \boldsymbol{j} - \sin\theta_5 \boldsymbol{k} \end{cases} \tag{22}$$

The drag coefficient of the pectoral fins is similar to that of the caudal fin [32]:

$$C_{Di} = 15.4 \times Re^{-0.4} = 15.4 \times \left(\frac{2r_y \boldsymbol{V}_i}{\mu}\right)^{-0.4} \tag{23}$$

Similar to the caudal fin, the lift and drag acting on the robotic pectoral fins are expressed in body coordinates as:

$$\boldsymbol{F}_{Li} = R_{ki} F'_{Li} \widehat{\boldsymbol{V}}_i \tag{24}$$

$$\boldsymbol{F}_{Di} = -F'_{Di} \boldsymbol{n}_i \tag{25}$$

where R_{ki} is the rotation matrix and $\widehat{\boldsymbol{V}}_i$ is the vector normal to $\boldsymbol{V}_i$.

Therefore, the moment acting on the pectoral fins can be written as:

$$\boldsymbol{M}_i = \boldsymbol{r}_i \times (\boldsymbol{F}_{Li} + \boldsymbol{F}_{Di}) \tag{26}$$

3) FORCE ANALYSIS OF THE HEAD

The pitch and yaw joints of the head are only used for mobility during the movement of the robotic dolphin, and the power generated by the head movement can be overlooked, which is only affected by the resistance and resisting moment generated during the relative flow movement of the robotic dolphin. It easily follows that:

$$\boldsymbol{F}_h = -\frac{1}{2}\rho C_{Dh} |\boldsymbol{V}|^2 S_h \widehat{\boldsymbol{V}} \tag{27}$$

$$C_{Dh} = 15.4 \times \left(\frac{(L_0 + L_1)\boldsymbol{V}}{\mu}\right)^{-0.4} \tag{28}$$

where C_{Dh} is the drag coefficient of the head, S_h is its surface area, and $\widehat{\boldsymbol{V}}$ is the vector normal to $\boldsymbol{V}$.

The resisting moment generated by the head is represented as:

$$\boldsymbol{M}_h = \boldsymbol{r}_h \times \boldsymbol{F}_h \tag{29}$$

where $\boldsymbol{r}_h$ is the position of the head centroid in the body coordinate system, which can be described as:

$$\boldsymbol{r}_h = \begin{bmatrix} \frac{1}{2}(L_0 - L_1)\cos\theta_6 \cos\theta_7 + L_1 \cos\theta_6 + L_2 \\ \frac{1}{2}(L_0 - L_1)\sin\theta_7 \\ \frac{1}{2}(L_0 + L_1)\sin\theta_6 \end{bmatrix} \tag{30}$$

where θ_6 represents the yaw joint angle and θ_7 the pitch joint angle.

4) FORCE ANALYSIS OF THE BODY

The robotic dolphin is affected by body resistance at low speed and high Reynolds number. The drag acting on the robotic body is expressed as [26]:

$$F_{D4} = -\frac{1}{2}\rho C_D |\boldsymbol{V}|^2 S_h \widehat{\boldsymbol{V}} \tag{31}$$

$$C_{D4} = 15.4 \times \left(\frac{L\boldsymbol{V}}{\mu}\right)^{-0.4} \tag{32}$$

where C_{D4} is the resistance coefficient of the body and S is its surface area.

Its resisting moment is:

$$\boldsymbol{M}_{D4} = -K_D \boldsymbol{\omega}^2 sgn(\boldsymbol{\omega}) \tag{33}$$

where K_D is the coefficient of the resisting moment.

5) GRAVITY AND BUOYANCY OF THE BODY

The points where gravity and buoyancy act on the robotic dolphin are on the same straight line and parallel to the y-axis. The distance is $\boldsymbol{r}_B = (0, y_B, 0)^T$. In the body coordinate system, the gravity and buoyancy are expressed as follows:

$$\boldsymbol{F}_G = {}^G_0 R \boldsymbol{G} \tag{34}$$

$$\boldsymbol{F}_B = {}^G_0 R \boldsymbol{B} \tag{35}$$

where $\boldsymbol{G} = (0, -m_b g, 0)^T$ is the gravity acting on the robotic dolphin, $\boldsymbol{B} = (0, \rho g V_B, 0)^T$ is the buoyancy acting on the robotic dolphin, and V_B is the volume of the robotic dolphin.

With the ground coordinate system as the reference system and the fish-body coordinate system as the motional system, the coordinate transformation matrix is given by:

$${}^0_G R = \begin{bmatrix} c\gamma s\varphi & c\gamma s\varphi s\psi - s\gamma c\psi & c\gamma s\varphi c\psi + s\gamma s\psi \\ s\gamma c\varphi & s\gamma s\varphi s\psi + c\gamma c\psi & s\gamma s\varphi c\psi - c\gamma s\psi \\ -s\varphi & c\varphi s\psi & c\varphi c\psi \end{bmatrix} \tag{36}$$

where $c\gamma$ represents $\cos\gamma$, $s\gamma$ represents $\sin\gamma$, etc.

Then, the coordinate transformation matrix with the body coordinate system as the reference system is:

$$ {}^{G}_{0}R = {}^{0}_{G}R^{T} \tag{37} $$

The moments generated by gravity and buoyancy are:

$$ \boldsymbol{M}_G = \widehat{r}_G \times \boldsymbol{F}_G \tag{38} $$

$$ \boldsymbol{M}_B = \boldsymbol{r}_B \times \boldsymbol{F}_B \tag{39} $$

where $\widehat{r}_G = \begin{bmatrix} 0 & -Z & Y \\ Z & 0 & -X \\ -Y & X & 0 \end{bmatrix}$.

For the angular velocity, the coordinate transformation matrix with the ground coordinate system as the reference system can be expressed as:

$$ {}^{0}_{G}T = \begin{bmatrix} 0 & \cot\varphi\sin\psi & \cot\varphi\cos\psi \\ 0 & \cos\psi & -\sin\psi \\ 1 & \tan\varphi\sin\psi & \tan\varphi\cos\psi \end{bmatrix} \tag{40} $$

6) FLUID INERTIA FORCE

The robotic dolphin is also affected by the inertial force from the fluid during movement, resulting in added mass.

The momentum and moment of momentum of the fluid are given as:

$$ \begin{cases} P = -\int \rho\phi \boldsymbol{n}_s \mathrm{d}s \\ K = -\int \rho(\boldsymbol{r} \times \boldsymbol{n}_s)\phi \mathrm{d}s \end{cases} \tag{41} $$

where ϕ is the velocity potential of the fluid, $\boldsymbol{r}$ is the radius vector of any point of the fluid, and $\boldsymbol{n}_s$ is the vector normal to the wetted area of the robotic dolphin.

The boundary condition of an ideal fluid is written as [30]:

$$ \frac{\partial\phi}{\partial \boldsymbol{n}_s}|_s = (\boldsymbol{V} + \boldsymbol{\omega} \times \boldsymbol{r}) \cdot \boldsymbol{n}_s \tag{42} $$

According to the Kirchhoff laws [31], the velocity potential function can be expressed as:

$$ \phi = V_x\sigma_1 + V_y\sigma_2 + V_z\sigma_3 + \omega_x\sigma_4 + \omega_y\sigma_5 + \omega_z\sigma_6 \tag{43} $$

where σ_i is a function of the unit velocity potential.

The expression of the added mass can be obtained from equations (41)-(43):

$$ m_{aij} = -\int \rho\sigma_j \frac{\partial\sigma_i}{\partial \boldsymbol{n}_s} dS \tag{44} $$

where $i = 1, 2, 3, 4, 5, 6$ and $j = 1, 2, 3, 4, 5, 6$.

The structure of the robotic dolphin is symmetrical about the $x_0o_0y_0$ plane, and the added mass on the nonleading diagonal can be ignored. Therefore, the added mass matrix can be simplified as:

$$ m_a = diag(m_{a11}, m_{a22}, m_{a33}, m_{a44}, m_{a55}, m_{a66}) \tag{45} $$

As a result, the external forces and moments on the robotic dolphin in all directions and its moment are described as follows:

$$ \begin{cases} F_x = \sum_{i=1}^{3} F_{Lix} + F_{hx} + \sum_{i=1}^{4} F_{Dix} + F_{px} + F_{Gx} + F_{Bx} \\ F_y = \sum_{i=1}^{3} F_{Liy} + F_{hy} + \sum_{i=1}^{4} F_{Diy} + F_{py} + F_{Gy} + F_{By} \\ F_z = \sum_{i=1}^{3} F_{Liz} + F_{hz} + \sum_{i=1}^{4} F_{Diz} + F_{pz} + F_{Gz} + F_{Bz} \\ M_x = \sum_{i=1}^{4} M_{ix} + M_{hx} + M_{Gx} + M_{Bx} \\ M_y = \sum_{i=1}^{4} M_{iy} + M_{hy} + M_{Gy} + M_{By} \\ M_z = \sum_{i=1}^{4} M_{iz} + M_{hz} + M_{Gz} + M_{Bz} \end{cases} \tag{46} $$

C. DYNAMIC EQUATIONS

There are generally five typical methods for dynamic model development: the Newton–Euler formulation, Kane's method, Lagrange method, Morison equation and strip method, and the Navier–Stokes equations. Based on the principle of force balance, the Newton-Euler method is simple and fast in calculation [32]. Kane established the kinetic equation with the generalized velocity as the generalized coordinates, which is applicable to both holonomic and nonholonomic systems [33]. The Lagrange method is simple in derivation but complex in calculation and is only applicable to robotic fish with fewer joints [34]. The Morrison method is simple and intuitive but not suitable for large robotic fish [35]. The Navier–Stokes equation is accurate in calculation, but it takes a long time [16]. Therefore, this paper uses the Newton-Euler equation to model the dynamics of the robotic dolphin.

$$ \begin{bmatrix} m & 0 \\ 0 & J \end{bmatrix} \begin{bmatrix} \dot{\boldsymbol{V}} \\ \dot{\boldsymbol{\omega}} \end{bmatrix} + \begin{bmatrix} \dot{\boldsymbol{\omega}} \times m\boldsymbol{V} \\ \dot{\boldsymbol{\omega}} \times J\boldsymbol{V} \end{bmatrix} = \begin{bmatrix} \boldsymbol{F} \\ \boldsymbol{M} \end{bmatrix} \tag{47} $$

where m is the mass matrix, including the mass m_b and added mass $m_a$of the robotic dolphin, and J is the inertia matrix, including the rotational inertia J_b and added inertia J_a of the robotic dolphin. Then, $m_a = diag(m_{a11}, m_{a22}, m_{a33})$, $J_b = diag(J_{xx}, J_{yy}, J_{zz})$, $J_a = diag(m_{a44}, m_{a55}, m_{a66})$. Finally, the model for the robotic fish can be further summarized to the control-affine form:

$$ \begin{cases} m_x\dot{V}_x = m_y\omega_z V_y - m_z\omega_y V_z + F_x \\ m_y\dot{V}_y = m_z\omega_x V_z - m_x\omega_z V_x + F_y \\ m_z\dot{V}_z = m_x\omega_y V_x - m_y\omega_x V_y + F_z \\ J_x\dot{\omega}_x = (J_y - J_z)\omega_y\omega_z + M_x \\ J_y\dot{\omega}_y = (J_z - J_x)\omega_z\omega_x + M_y \\ J_z\dot{\omega}_z = (J_x - J_y)\omega_x\omega_y + M_z \end{cases} \tag{48} $$

where $m_x = m_b + m_{a11}$, $m_y = m_b + m_{a22}$, $m_z = m_b + m_{a33}$, $J_x = J_{xx} + m_{a44}$, $J_y = J_{yy} + m_{a55}$, and $J_z = J_{zz} + m_{a66}$.

Now, we can obtain the kinematics model in the inertial coordinates from equations (36) and (40):

$$\begin{cases} \begin{bmatrix} \dot{X} \\ \dot{Y} \\ \dot{Z} \end{bmatrix} = {}^{0}_{G}R \begin{bmatrix} V_x \\ V_y \\ V_z \end{bmatrix} \\ \begin{bmatrix} \dot{\psi} \\ \dot{\varphi} \\ \dot{\gamma} \end{bmatrix} = {}^{0}_{G}T \begin{bmatrix} \omega_x \\ \omega_y \\ \omega_z \end{bmatrix} \end{cases} \tag{49}$$

This paper mainly studies the turning maneuverability of the robotic dolphin on the $x_0o_0z_0$ surface. We can make $Y = 0$, $V_y = 0$, $\omega_x = \omega_z = 0$, $\psi = \gamma = 0$, so equations (48)-(49) can be evaluated as:

$$\begin{cases} m_x\dot{V}_x = F_x - m_z\omega_y V_z \\ m_z\dot{V}_z = F_z + m_x\omega_y V_x \\ J_y\dot{\omega}_x = M_y \\ \dot{X} = V_x\cos\varphi + V_z\sin\varphi \\ \dot{Z} = V_Z\cos\varphi - V_x\sin\varphi \\ \dot{\varphi} = \omega_y \end{cases} \tag{50}$$

IV. SIMULATION AND EXPERIMENTAL RESULTS

In this section, various turning patterns are simulated and analyzed, and to evaluate the effectiveness of the developed dynamic model, multimodal swimming behaviors, including flapping-wing turning, swinging-wing turning, head-offset turning, and head-flipper synergetic turning, are extensively investigated. Specifically, the motion parameters include the swing frequency of the pectoral fins and the offset angle of the head, and the maneuverability evaluation indexes cover the turning angular velocity and turning radius.

A. EXPERIMENTAL SETUP AND MODEL PARAMETERS

The turning motions in different patterns are performed in a 6.0 m × 4.0 m × 1.5 m tank. The experimental setup is shown in Fig. 4. To obtain the swimming posture and motion parameters of the robotic dolphin more accurately, a set of online tracking systems based on infrared motion capture cameras is built. The online tracking system is made up of 8 motion capture cameras, mark points, a static calibration board, a dynamic calibration rod, and a computer. The motion capture cameras make use of a twisted pair to connect to the computer through a network switch to realize data transmission and power supply. Eight cameras are successively fixed 2.1 meters away from the water surface according to their numbers. In particular, the mark points adhere to the robotic dolphin so that the motion capture cameras can capture the motion state of the mark points to obtain the swimming posture and motion parameters of the robotic dolphin. The static calibration board and dynamic calibration rod are also pasted with mark points, which are mainly used to determine the global coordinate system of the online tracking system. The computer is used to receive and process the data transmitted by the motion capture camera.

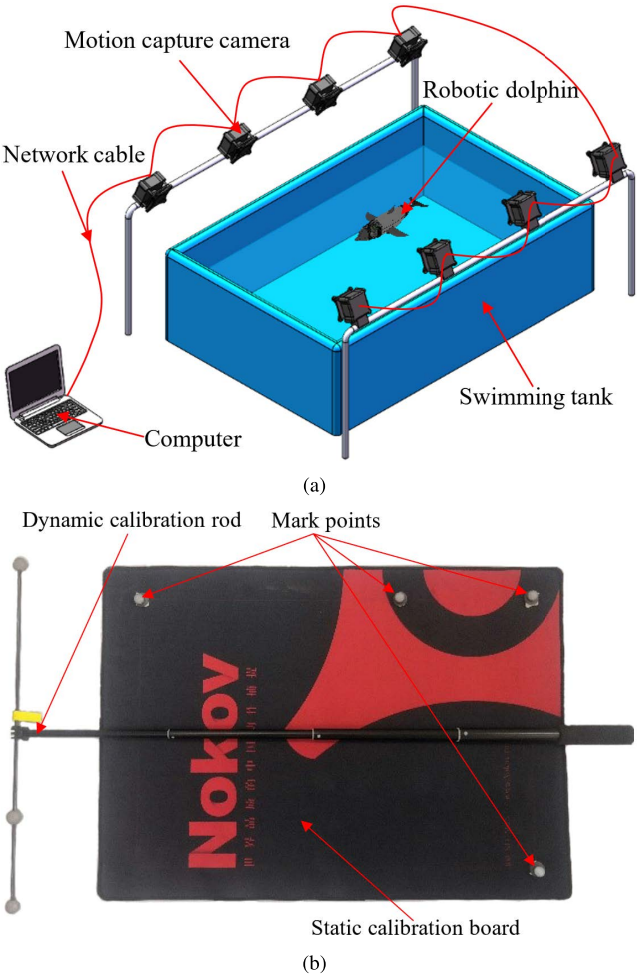

FIGURE 4. Experimental platform. (a) Perimental setup. (b) Static and dynamic calibration systems.

Prior to simulation and experiment, we needed to determine some basic parameters of the robotic dolphin. ρ and μ are the density and viscosity coefficient of water, respectively. Some parameters can be obtained by simple measurement, such as the mass of the robotic dolphin, the length of each joint, and the distance to the centroid, while others can be obtained by calculation, such as the rotational inertia, added mass, wetted area of the robotic dolphin, etc.

The m_b is determined using an electronic scale. Each joint and the distance to the centroid, such as L_0, L_1, L_2, C_x, p_x, p_z, q_x, r_y, and r_z, are measured with a scale. We calculate S, S_1, S_2, and S_h using three-dimensional software. The robotic dolphin is approximated as an ellipsoid, and its moment of inertia is calculated as follows [36]:

$$\begin{cases} J_{xx} = 0.2m_b(H^2 + W^2) \\ J_{yy} = 0.2m_b(W^2 + L^2) \\ J_{zz} = 0.2m_b(L^2 + H^2) \end{cases} \tag{51}$$

The added mass and moments are calculated according to the literature [37] and equation (44), where m_{a11}, m_{a22}, and m_{a33} are the added mass in kg, and m_{a44}, m_{a55}, and m_{a66} are

the added mass moments in $kg \cdot m^2$. These basic parameters are given in Table 2.

TABLE 2. Parameter values for the model.

Item	Value	Item	Value
m_b	15.020 kg	S	0.735 m^2
m_{a11}	1.459 kg	ρ	1000 kg$\cdot$ m^{-3}
m_{a22}	20.728 kg	μ	10^{-6} $m^2\cdot$ s
m_{a33}	20.728 kg	L_0	0.190 m
m_{a44}	0.001 kg$\cdot$ m^2	L_1	0.080 m
m_{a55}	0.850 kg$\cdot$ m^2	L_2	0.210 m
m_{a66}	0.850 kg$\cdot$ m^2	C_x	0.225 m
J_{xx}	0.363 kg$\cdot$ m^2	p_x	0.120 m
J_{yy}	3.266 kg$\cdot$ m^2	p_z	0.140 m
J_{zz}	3.238 kg$\cdot$ m^2	q_x	0.250 m
S_1	0.083 m^2	r_y	0.100 m
S_2	0.020 m^2	r_z	0.050 m
S_h	0.171 m^2		

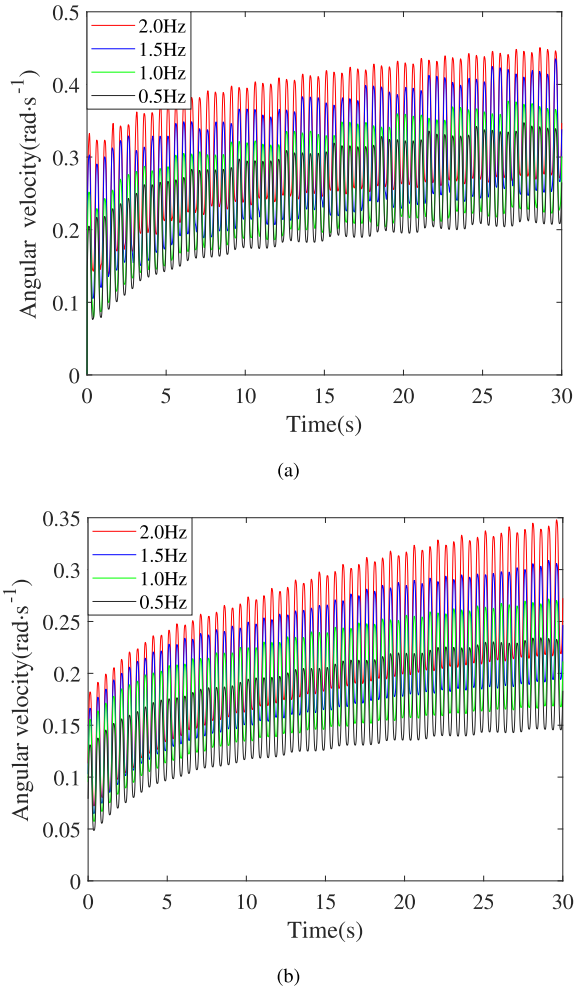

FIGURE 5. Angular velocity of the pectoral-fin turning patterns. (a) Pattern I. (b) Pattern II.

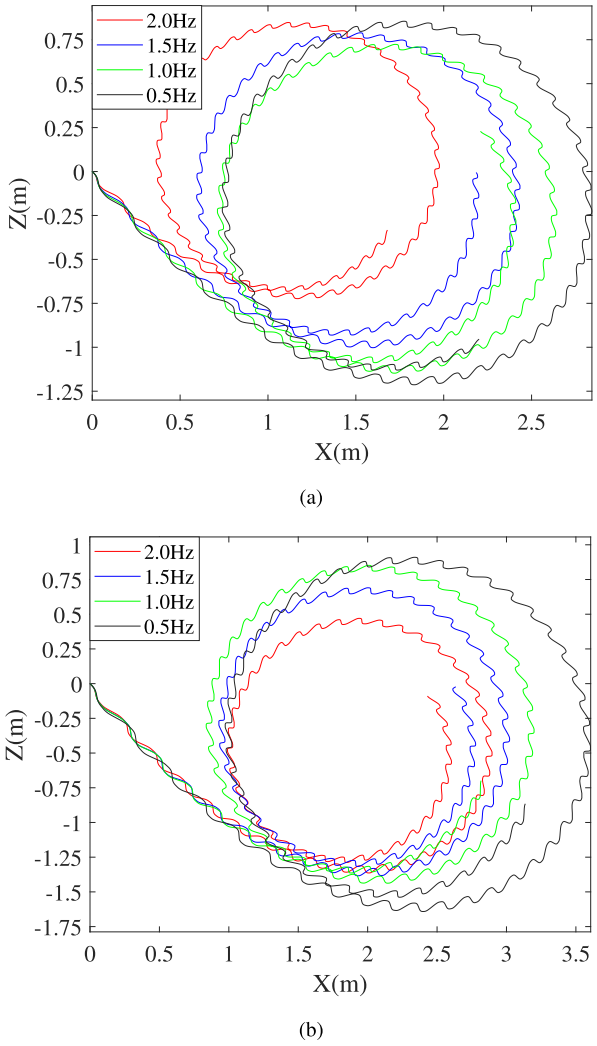

FIGURE 6. Turning radii of the pectoral-fin turning patterns. (a) Pattern I. (b) Pattern II.

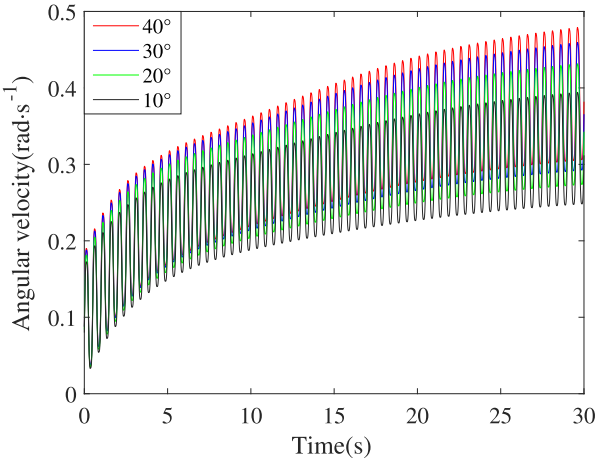

FIGURE 7. Angular velocity of the head-offset turning pattern.

B. SIMULATION OF THE TURNING MOTIONS

We will study the relationship between the motion parameters, including the frequency of the pectoral fins and the head-offset angle, and the evaluation indexes of mobility, including the turning angular velocity and radius, using simulation.

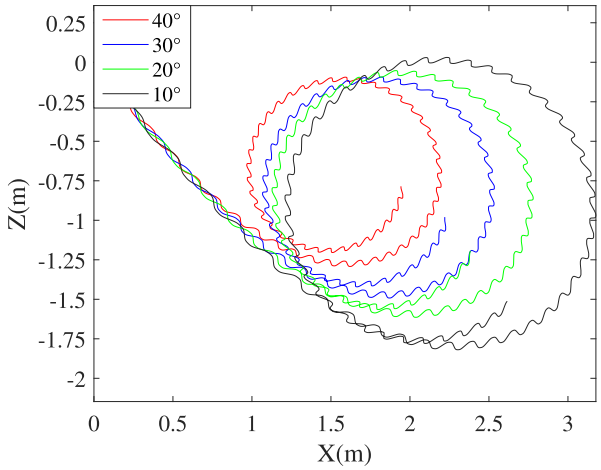

FIGURE 8. Turning radii of the head-offset turning pattern.

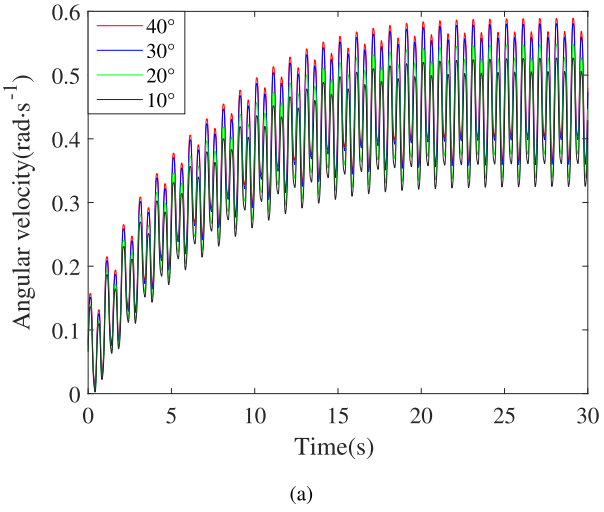

(a)

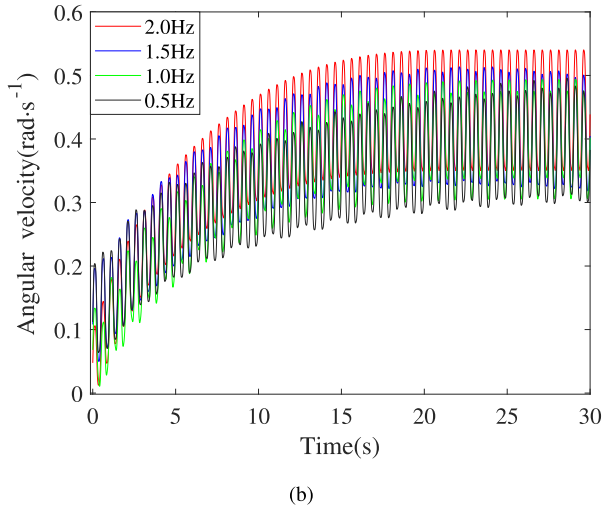

(b)

FIGURE 9. Angular velocities of the cooperative turning patterns. (a) Pattern IV-a. (b) Pattern IV-b.

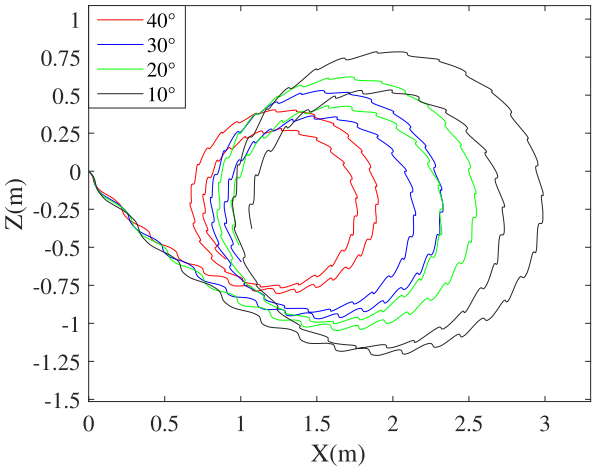

(a)

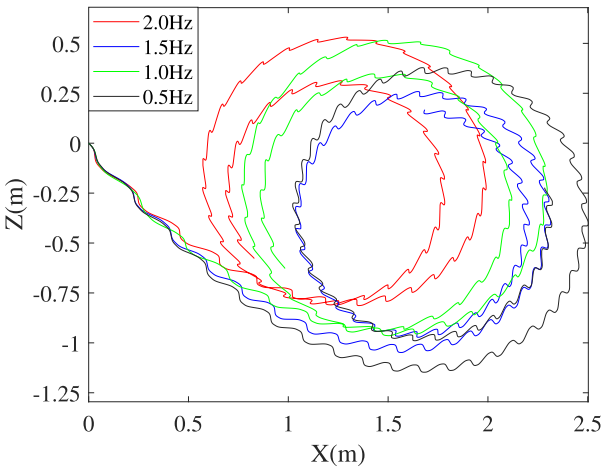

(b)

FIGURE 10. Turning radii of the cooperative turning patterns. (a) Pattern IV-a. (b) Pattern IV-b.

1) TURNING WITH FLIPPERS

Turning with pectoral fins is mainly inclusive of Patterns I and II. In the simulation, we separately examine the effects of the swing frequency of the pectoral flapping joint and swinging joint on the turning angular velocity and turning radius. The evaluated swing frequencies are 0.5 Hz, 1.0 Hz, 1.5 Hz, and 2.0 Hz. Fig. 5 shows the turning angular velocity of Patterns I and II at different frequencies. We can observe that the turning angular velocity increases with the swing frequency of the pectoral fins. 0.2478 rad/s and 0.3310 rad/s are the average values of the minimum and maximum turning angular velocities of Pattern I, respectively, and 0.1585 rad/s and 0.2278 rad/s are the average values of the minimum and the maximum turning angular velocities of Pattern II, respectively. As the results indicate, the turning angular velocity of the flapping pattern exceeds that of the swinging pattern under the same frequency. Fig. 6 shows the turning radii of Patterns I and II at different frequencies. We can see that the turning radius of the robotic dolphin decreases with increasing flipper frequency. 0.7569 m and 0.9752 m are, respectively, the minimum and maximum turning radii of Pattern I, and 0.8789 m and 1.2010 m are, respectively, the minimum and maximum turning radii of Pattern II. Therefore,

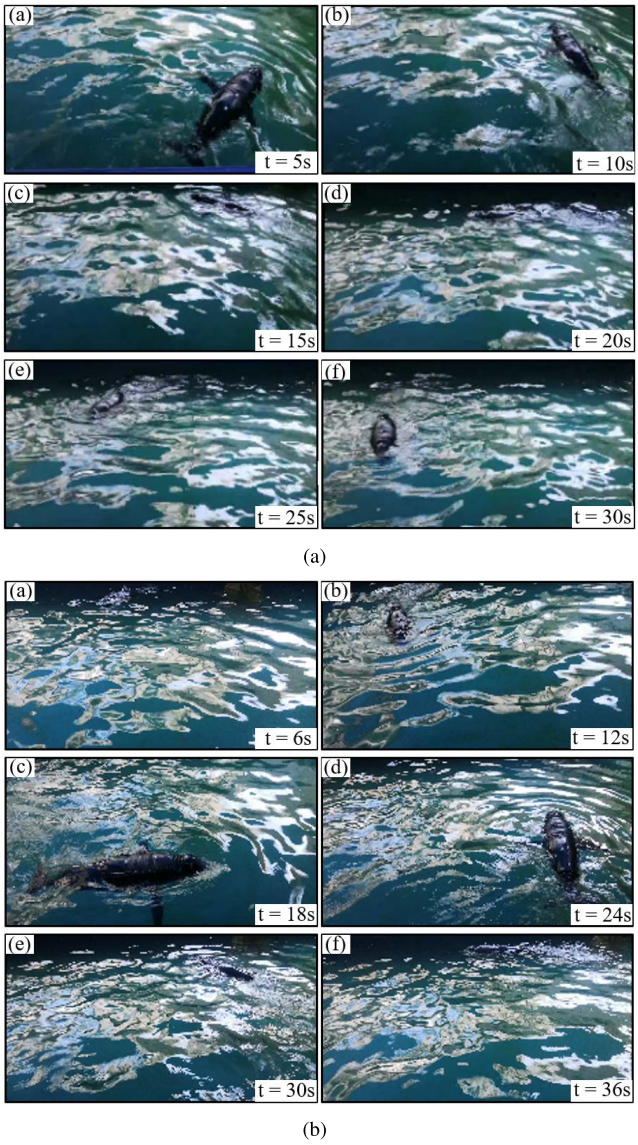

FIGURE 11. Experimental snapshots of the robotic dolphin using the pectoral-fin turning patterns. (a) Pattern I. (b) Pattern II.

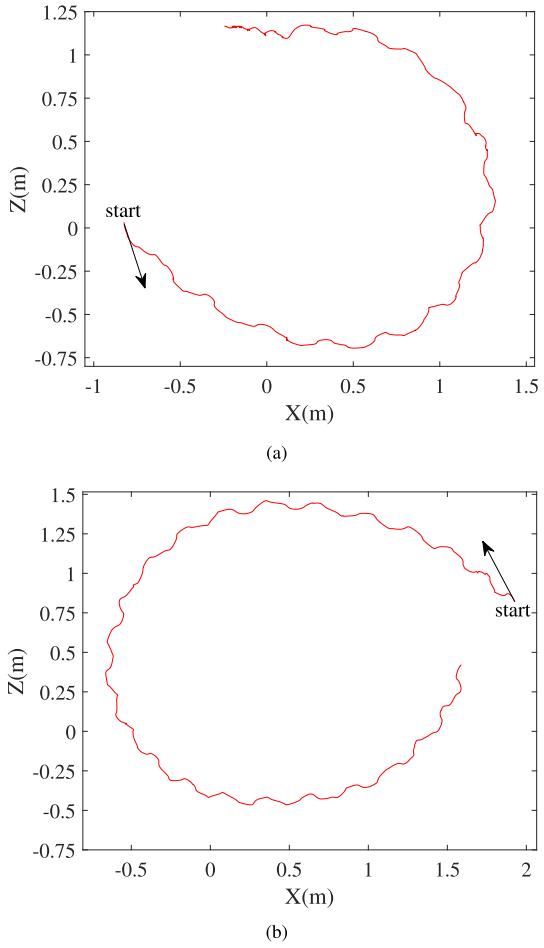

FIGURE 12. Experimental results of performing a turning trajectory with the pectoral-fin turning patterns. (a) Pattern I. (b) Pattern II.

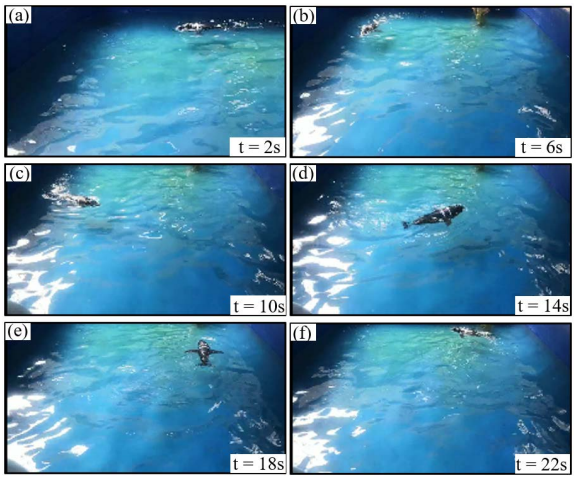

FIGURE 13. Experimental snapshots of the robotic dolphin with the head-offset turning pattern.

the turning radius of the flapping-wing pattern is smaller than that of the swinging-wing pattern at the same frequency.

2) TURNING WITH THE HEAD

For the head-offset turning pattern, we study the influence of the head-offset angle on the turning performance. Due to the limitation of the mechanical structure, the deflection angle range of the robotic dolphin head is [-40°, 40°], and the evaluated operating conditions for the offset angle of the head are 10°, 20°, 30°, and 40°. The turning angular velocity of Pattern III under different deflection angles is shown in Fig. 7. We can see that the turning angular velocity increases with the head deflection angle, and the average values of its minimum and maximum turning angular velocity are 0.3066 rad/s and 0.3735 rad/s, respectively. Fig. 8 shows the turning radius of Pattern III under different deflection angles. As the simulation results indicate, the turning radius decreases with increasing head deflection angle, and the minimum and maximum turning radii are 0.5988 m and 0.9095 m, respectively.

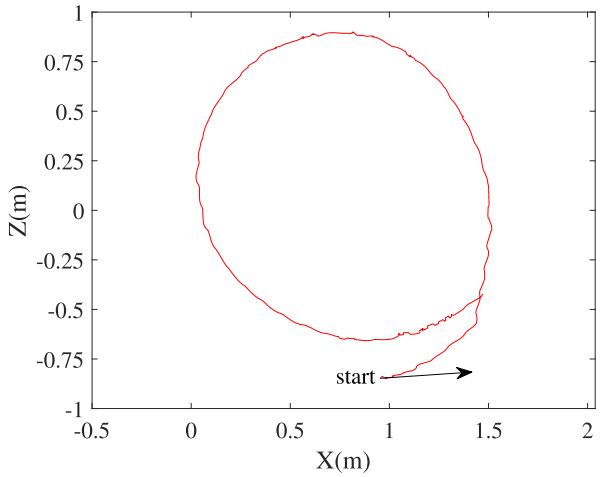

FIGURE 14. Experimental results of performing a turning trajectory with the head-offset turning pattern.

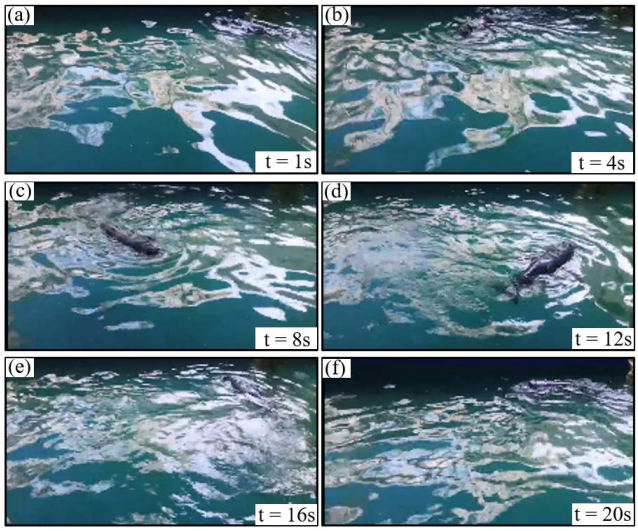

FIGURE 15. Experimental snapshots of the dolphin robot with the cooperative turning pattern.

3) TURNING WITH HEAD-FLIPPERS COORDINATION

The synergic turning simulation is divided into two groups. One keeps the pectoral-fin swing frequency at 1 Hz and change the head-offset angle, which is recorded as Pattern IV-a, and the other keeps the head deflection angle at 30° and changes the pectoral-fin swing frequency, which is recorded as Pattern IV-b. Fig. 9 shows the angular velocities of the synergic turning patterns. Fig. 9 (a) shows the turning angular velocity under different head deflection angles when the frequency is 1 Hz and that the average values of the minimum and maximum turning angular velocities are 0.3525 rad/s and 0.4190 rad/s, respectively. Fig. 9 (b) shows the turning angular velocity under different frequencies when the head deflection angle is 30° and that the average values of the minimum and the maximum turning angular velocities are 0.3665 rad/s and 0.4359 rad/s, respectively.

Fig. 10 shows the turning radii of the synergic turning patterns. Fig. 10 (a) shows the turning radius under different head deflection angles when the frequency of the pectoral fins is 1 Hz and that the minimum and maximum turning radii are 0.5132 m and 0.8609 m, respectively. Fig. 10 (b) shows the turning radius under different frequencies when the head deflection angle is 30° and that the minimum and maximum turning radii are 0.5569 m and 0.6842 m, respectively. For the turning radius, the influence of the head deflection angle exceeds that of the pectoral-fin swing frequency, and for the turning angular velocity, the frequency has a stronger influence than the head deflection angle.

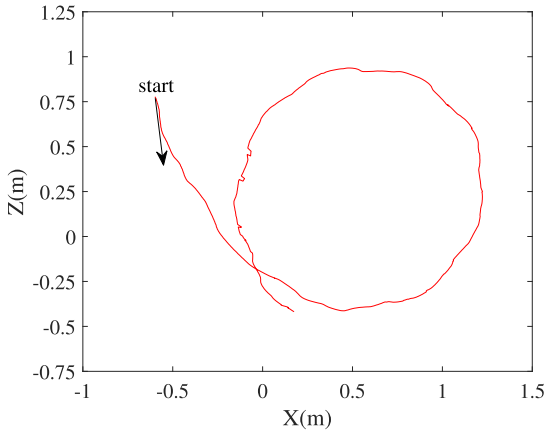

FIGURE 16. Experimental results of performing a turning trajectory with the cooperative turning pattern.

The simulation results indicate that, in comparison with a single turning pattern, the synergic turning pattern has a smaller turning radius and a larger turning angular velocity.

C. EXPERIMENTAL RESULTS

To validate the correctness and effectiveness of the simulation models for the four turning patterns, we conducted a large number of experiments.

1) TESTING OF TURNING WITH THE FLIPPERS

Fig. 11 shows the sequence diagram of the pectoral-fin turning patterns. Fig. 11 (a) and Fig. 11 (b) represent the turning conditions of the flapping-wing pattern and the swinging-wing pattern, respectively, in which the pectoral-fin frequency of the flapping-wing pattern is 0.5 Hz and that of the swinging-wing pattern is 2 Hz. As shown in the turning trajectory chart captured by the motion capture camera, the actual turning radii of Patterns I and II are 1.0727 m and 0.9567 m, respectively, and according to the swimming time, the turning angular velocities are 0.1974 rad/s and 0.1916 rad/s, respectively.

2) TESTING OF TURNING WITH THE HEAD

The sequence diagram of the head-offset pattern is shown in Fig. 13, and the head offset angle is 20°. We can observe from the turning trajectory chart captured by the motion capture cameras, shown in Fig. 14, that the turning radius is 0.8436 m, and we can determine according to the swimming time that the turning angular velocity is 0.3260 rad/s.

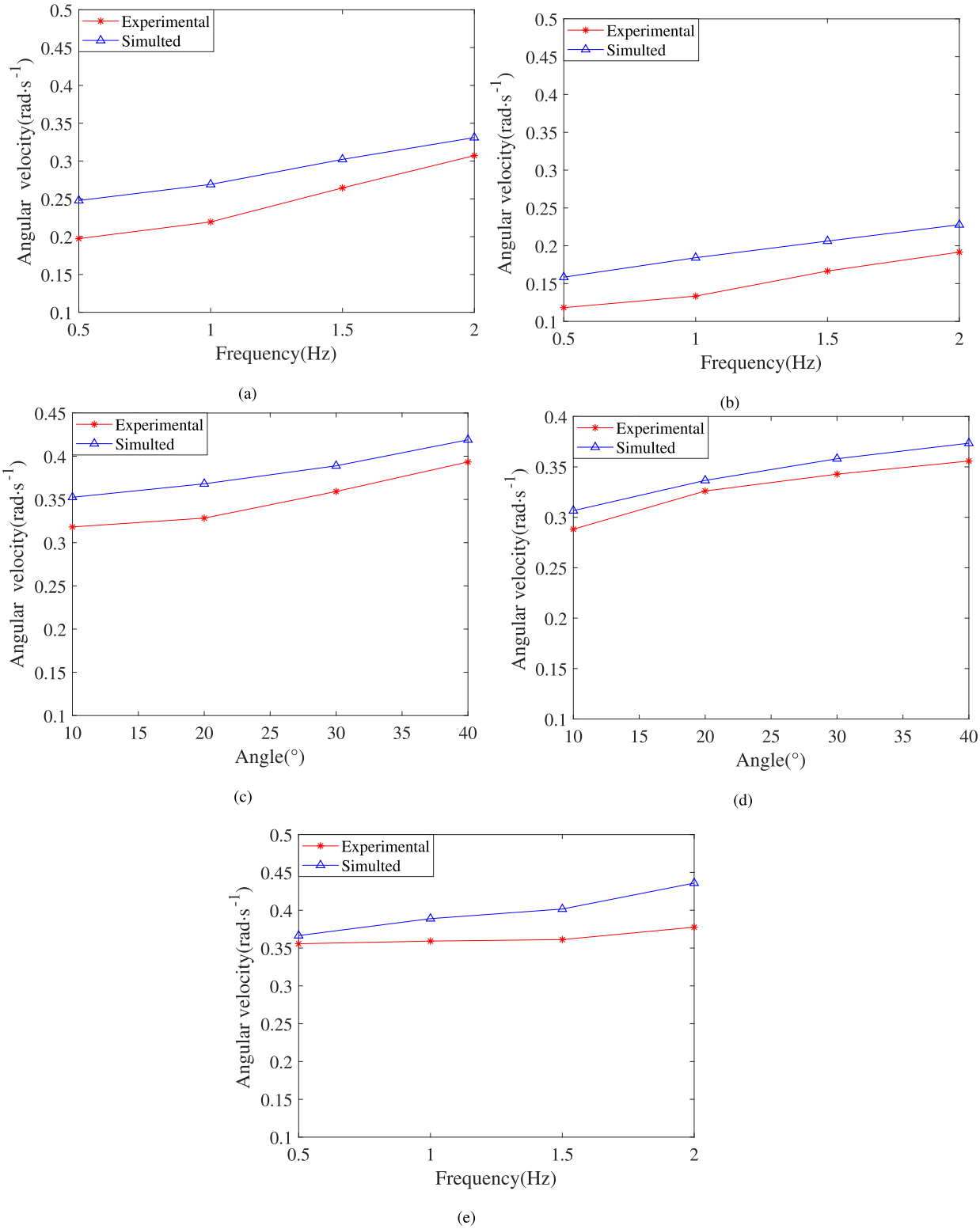

FIGURE 17. Comparative evaluations of the angular velocities. (a) Pattern I. (b) Pattern II. (c) Pattern III. (d) Pattern IV-a. (e) Pattern IV-b.

3) TESTING OF TURNING WITH HEAD-FLIPPERS COORDINATION

The sequence diagram of the cooperative turning pattern is shown in Fig. 15. The head deflection angle is 30°, and the frequency is 1 Hz. From the turning trajectory chart captured by the motion capture cameras, shown in Fig. 16, we can observe that the turning radius is 0.6744 m, and the turning angular velocity is 0.3592 rad/s according to the

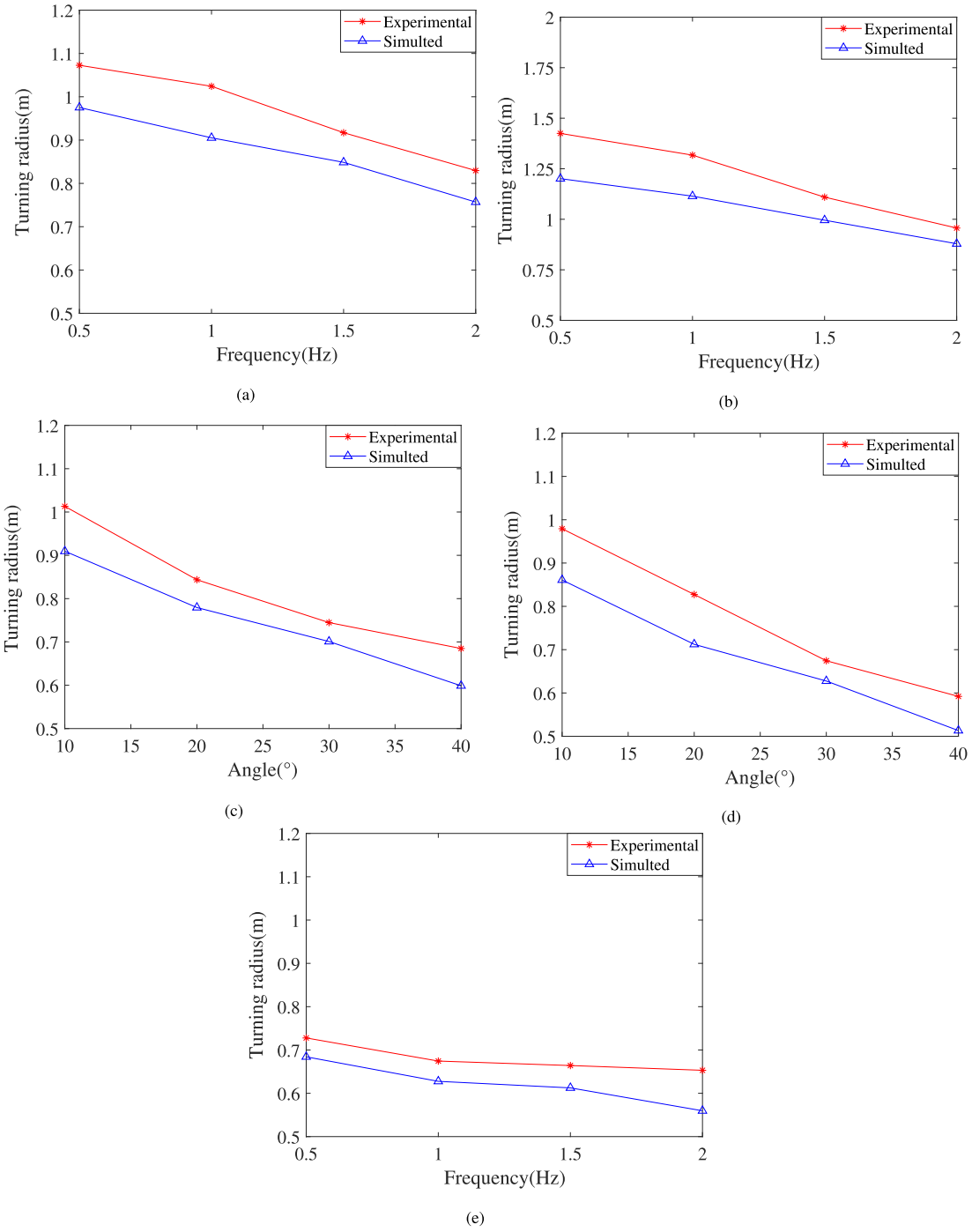

FIGURE 18. Comparative evaluations of the turning radii.(a) Pattern I. (b) Pattern II.(c) Pattern III. (d) Pattern IV-a. (e) Pattern IV-b.

swimming time. We can see from the experimental results that the cooperative pattern exceeds a single pattern in turning performance.

Figs. 17 and 18 are the comparison diagrams of the simulation and experiments for the turning angular velocity and turning radius, respectively, under the four turning patterns. From such comparisons, we can see that the turning angular velocity obtained by simulation is larger than the experimental results and that the turning radius is smaller than the experimental value. The main reasons are as follows. 1) The energy loss of the driving mechanism. The working principle of the tail drive mechanism is that a four-bar mechanism brings about the sinusoidal swing of the caudal fin under the drive of two motors. In the movement process, the mechanism idles due to friction and the assembly error also causes a certain energy loss. Also, the pectoral fins and head are driven by steering gears, which cannot produce enough torque due to large resistance. 2) Sealing method. Skin sealing can be used to improve waterproof performance, but it will increase the resistance of the robotic dolphin when

swimming. 3) Head vibration. When the caudal fin moves up and down, it will cause a pitching torque, making the head vibrate in the vertical plane. 4) Surge effect. The robotic dolphin will produce waves when moving. Limited by the size of the tank, such waves will spread to the robotic dolphin from the wall surface, increasing its forward resistance.

D. DISCUSSION

Inspired by natural dolphins, scholars have developed various types of robotic dolphins. The up-down movement of the caudal fin that produces the main propulsive force of robotic dolphins is unable to provide the power required for turning, which means robotic dolphins depend on the pectoral fins for turning, and the turning maneuverability is finite. The turning performance is effectively improved through the use of head yaw joints. In particular, the head-flippers synergic turning pattern can lessen the turning radius and increase the turning angular velocity. In addition, the pectoral fins have two degrees of freedom and can make flapping-wing and swinging-wing turns. As the pectoral-fin swing frequency rises, the turning radius decreases, and the turning angular velocity increases. In addition, the turning performance of the flapping-wing pattern surpasses that of the swinging-wing pattern. The larger the head deflection angle is, the better the turning performance of the robotic dolphin will be, and the turning radius is smaller than that of turning with the pectoral fins.

On the other hand, to reflect the advantages of the synergic turning pattern proposed in this study, a comparison with the turning performance of other robotic fish is shown in Table 3. Generally, the turning radius of robotic fish is closely related to the body length. To eliminate the influence of body length, the turning radius here is defined as the actual turning radius longer than the upper body length. We can see that the turning radius and turning angular velocity in the synergic turning pattern have certain competitiveness. Of course, there is still a certain gap between the robotic dolphins and natural dolphins in turning mobility due to the rigid body of the former. Therefore, in future work, it will be a challenging to improve the turning maneuverability with soft bodies.

TABLE 3. The turning comparison of several methods.

Reference	Average turning velocity	Turning radius
Ref. [18]	0.24 rad/s	1.07 BL
Ref. [21]	-	0.93 BL
Ref. [22]	0.02 rad/s	0.93 BL
Ref. [23]	0.34 rad/s	2.06 BL
Present study	0.39 rad/s	0.58 BL

V. CONCLUSION AND FUTURE WORK

Turning maneuverability is a critical performance index of bionic robotic dolphins. However, robotic dolphins cannot rely on the caudal fin that produces the main propulsion to turn like a robotic fish, which greatly reduces the turning maneuverability of robotic dolphins. Therefore, we have developed a highly-maneuverable robotic dolphin with a yaw joint in the head, which can effectively improve the turning performance. First, by virtue of the advantage of multiple joints, we research four turning patterns of robotic dolphins, namely, flapping-wing turning pattern, swinging-wing turning pattern, head-offset turning pattern, and head-flipper collaborative turning pattern. Moreover, the latter two turning patterns were proposed for the first time. Second, for this type of robotic dolphin, we established a dynamic model for turning maneuverability and considered the effect of added mass acting on the robotic dolphin on the basis of quasi-steady hydrofoil theory and the Newton-Euler equation. Finally, we investigate four typical turning patterns using simulation and testing. As the simulation and experimental results demonstrate, a turning pattern using pectoral fins can increase the turning angular velocity, and a turning pattern using the head reduces the turning radius. Not only can a collaborative turning pattern increase the turning angular velocity, but it can also reduce the turning radius. In addition, extensive aquatic experiments validate the effectiveness of the developed dynamic model. This paper provides a reference for improving the turning maneuverability of underwater bionic robots in terms of structural design and dynamic modeling and provides a theoretical basis for turning maneuverability control.

Future work will concentrate on two aspects: optimizing the mechanical structure of robotic dolphins and making use of a more reasonable sealing method to further improve the mobility of the robotic dolphin; and testing the mobile performance evaluation of robotic dolphins by using a larger experimental site to conduct further verification and employing closed-loop control for target tracking to achieve more accurate control.

REFERENCES

[1] Q. Yan, W. Shang, and Q. Zhu, "Experimental study on the maneuverability of a robotic fish based on image processing," in *Proc. Int. Conf. Mech. Sci., Electr. Eng. Comput. (MEC)*, Dec. 2013, pp. 788–791.
[2] B. Pollard and P. Tallapragada, "Passive appendages improve the maneuverability of fishlike robots," *IEEE/ASME Trans. Mechtron.*, vol. 24, no. 4, pp. 1586–1596, Aug. 2019.
[3] Z. Yan, H. Yang, W. Zhang, Q. Gong, and F. Lin, "Research on motion mode switching method based on CPG network reconstruction," *IEEE Access*, vol. 8, pp. 224871–224883, 2020.
[4] C. Wang, J. Lu, X. Ding, C. Jiang, J. Yang, and J. Shen, "Design, modeling, control, and experiments for a fish-robot-based IoT platform to enable smart ocean," *IEEE Internet Things J.*, vol. 8, no. 11, pp. 9317–9329, Jun. 2021.
[5] J. Chen, B. Yin, C. Wang, F. Xie, R. Du, and Y. Zhong, "Bioinspired closed-loop CPG-based control of a robot fish for obstacle avoidance and direction tracking," *J. Bionic Eng.*, vol. 18, no. 1, pp. 171–183, Jan. 2021.
[6] X. Yi, A. Chakarvarthy, and Z. Chen, "Cooperative collision avoidance control of servo/IPMC driven robotic fish with back-relaxation effect," *IEEE Robot. Autom. Lett.*, vol. 6, no. 2, pp. 1816–1823, Apr. 2021.
[7] W. Wang and G. Xie, "Online high-precision probabilistic localization of robotic fish using visual and inertial cues," *IEEE Trans. Ind. Electron.*, vol. 62, no. 2, pp. 1113–1124, Feb. 2015.
[8] J. Yu, R. Ding, Q. Yang, M. Tan, W. Wang, and J. Zhang, "On a bio-inspired amphibious robot capable of multimodal motion," *IEEE/ASME Trans. Mechtron.*, vol. 17, no. 5, pp. 847–856, Oct. 2012.
[9] J. Wang, Z. Wu, S. Yan, M. Tan, and J. Yu, "Real-time path planning and following of a gliding robotic dolphin within a hierarchical framework," *IEEE Trans. Veh. Technol.*, vol. 70, no. 4, pp. 3243–3255, Apr. 2021.

[10] Y. S. Ryuh, G.-H. Yang, J. Liu, and H. Hu, "A school of robotic fish for mariculture monitoring in the sea coast," *J. Bionic Eng.*, vol. 12, no. 1, pp. 37–46, Jan. 2015.
[11] Z. Wu, J. Liu, J. Yu, and H. Fang, "Development of a novel robotic dolphin and its application to water quality monitoring," *IEEE/ASME Trans. Mechtron.*, vol. 22, no. 5, pp. 2130–2140, Oct. 2017.
[12] G. Taylor, "Analysis of the swimming of long and narrow animals," *Proc. Roy. Soc. London, A, Math. Phys. Sci.*, vol. 214, no. 1117, pp. 158–183, Aug. 1952.
[13] M. J. Lighthill, "Note on the swimming of slender fish," *J. Fluid Mech.*, vol. 9, no. 2, pp. 305–317, Oct. 1960.
[14] J. Y. Cheng, L. X. Zhuang, and B. G. Tong, "Analysis of swimming three-dimensional waving plates," *J. Fluid Mech.*, vol. 232, no. 1, pp. 341–355, Oct. 2006.
[15] F. Boyer, M. Porez, and W. Khalil, "Macro-continuous computed torque algorithm for a three-dimensional eel-like robot," *IEEE Trans. Robot.*, vol. 22, no. 4, pp. 763–775, Aug. 2006.
[16] J. Carling, T. L. Williams, and G. Bowtell, "Self-propelled anguilliform swimming: Simultaneous solution of the two-dimensional Navier–Stokes equations and Newton's laws of motion," *J. Experim. Biol.*, vol. 201, no. 23, pp. 3143–3166, Dec. 1998.
[17] J. Yu, S. Chen, Z. Wu, X. Chen, and M. Wang, "Energy analysis of a CPG-controlled miniature robotic fish," *J. Bionic Eng.*, vol. 15, no. 2, pp. 260–269, Mar. 2018.
[18] S. B. Behbahani and X. Tan, "Role of pectoral fin flexibility in robotic fish performance," *J. Nonlinear Sci.*, vol. 27, no. 4, pp. 1155–1181, Aug. 2017.
[19] S. Du, Z. Wu, and J. Yu, "Design and yaw control of a two-motor-actuated biomimetic robotic fish," in *Proc. IEEE Int. Conf. Robot. Biomimetics (ROBIO)*, Dec. 2019, pp. 126–131.
[20] J. Wang, Z. Wu, J. Liu, M. Tan, and J. Yu, "3-D motion analysis and implementation of a developed gliding robotic dolphin," in *Proc. IEEE Int. Conf. Robot. Biomimetics (ROBIO)*, Dec. 2019, pp. 1809–1814.
[21] J. Wang and X. Tan, "A dynamic model for tail-actuated robotic fish with drag coefficient adaptation," *Mechatronics*, vol. 23, no. 6, pp. 659–668, Sep. 2013.
[22] X. Li, Q. Ren, and J.-X. Xu, "An equilibrium-based learning approach with application to robotic fish," *Nonlinear Dyn.*, vol. 94, no. 4, pp. 2715–2725, Aug. 2018.
[23] X. Y. Chen, Z. X. Wu, C. Zhou, and J. Z. Yu, "Design and implementation of a magnetically actuated miniature robotic fish," *IFAC-PapersOnLine*, vol. 50, no. 1, pp. 6851–6856, Jul. 2017.
[24] A. Singh, A. Singla, and S. Soni, "Extension of D-H parameter method to hybrid manipulators used in robot-assisted surgery," *Proc. Inst. Mech. Eng., H, J. Eng. Med.*, vol. 229, no. 10, pp. 703–712, Sep. 2015.
[25] V. Kopman, J. Laut, F. Acquaviva, A. Rizzo, and M. Porfiri, "Dynamic modeling of a robotic fish propelled by a compliant tail," *IEEE J. Ocean. Eng.*, vol. 40, no. 1, pp. 209–221, Jan. 2015.
[26] M. Aureli, V. Kopman, and M. Porfiri, "Free-locomotion of underwater vehicles actuated by ionic polymer metal composites," *IEEE/ASME Trans. Mechtron.*, vol. 15, no. 4, pp. 603–614, Aug. 2010.
[27] H. Chen, C. A. Zhu, X. Z. Yin, X. Z. Xing, and Y. Zeng, "Dynamic simulation of swimming robot tuna based on Matlab," *J. Syst. Simul.*, vol. 18, no. 1, pp. 207–212, Jan. 2006.
[28] Y. X. Liu, J. K. Liu, and W. S. Chen, "The dynamic mode building and simulation of two-joint fish robot in no up and down movement," *Mech. Eng.*, vol. 5, no. 1, pp. 19–22, May 2007.
[29] A. J. Healey, S. M. Rock, S. Cody, D. Miles, and J. P. Brown, "Toward an improved understanding of thruster dynamics for underwater vehicles," *IEEE J. Ocean. Eng.*, vol. 20, no. 4, pp. 354–361, Oct. 1995.
[30] É. F. Rapoport, "Interaction of an elastic shell with two-dimensional flows of an ideal fluid," *Fluid Dyn.*, vol. 16, no. 5, pp. 751–754, Sep. 1981.
[31] H. S. Bhat and B. Osting, "Kirchhoff's laws as a finite volume method for the planar Maxwell equations," *IEEE Trans. Antennas Propag.*, vol. 59, no. 10, pp. 3772–3779, Oct. 2011.
[32] J. Yu, F. Sun, D. Xu, and M. Tan, "Embedded vision-guided 3-D tracking control for robotic fish," *IEEE Trans. Ind. Electron.*, vol. 63, no. 1, pp. 355–363, Jan. 2016.
[33] T. R. Kane and D. A. Levinson, "The use of Kane's dynamical equations in robotics," *Int. J. Robot. Res.*, vol. 2, no. 3, pp. 3–21, Sep. 1983.
[34] W.-K. Yen, D. M. Sierra, and J. Guo, "Controlling a robotic fish to swim along a wall using hydrodynamic pressure feedback," *IEEE J. Ocean. Eng.*, vol. 43, no. 2, pp. 369–380, Apr. 2018.
[35] J. Yu, J. Yuan, Z. Wu, and M. Tan, "Data-driven dynamic modeling for a swimming robotic fish," *IEEE Trans. Ind. Electron.*, vol. 63, no. 9, pp. 5632–5640, Sep. 2016.
[36] J. J. Zhou, Y. L. Yu, and Q. R. Xiang, "A numerical computation method of additional mass for underwater vehicle," *Torpedo Technol.*, vol. 21, no. 4, pp. 246–249, Apr. 2013.
[37] X. W. Zhao, B. C. Yang, and S. X. Huang, "Calculation of the rotary inertia of ellipsoid," *Phys. Eng.*, vol. 17, no. 2, pp. 28–29, Oct. 2007.

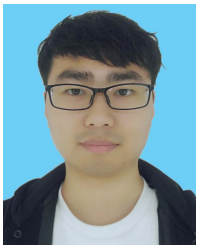

ZHONGHUA YANG was born in Xinyang, Henan, China, in 1995. He received the B.S. degree in mechanical design, manufacturing, and automation from Yangtze University, in 2017. He has been studying mechanical engineering at Shenzhen University, since 2019. His research interests include computational fluid dynamics and autonomous underwater vehicles.

WEIJIE GONG was born in Luohe, Henan, China, in July 1978. He received the Ph.D. degree in aircraft design from Northwestern Polytechnical University, China, in 2011. In 2011, he joined the College of Mechatronics and Control Engineer, Shenzhen University, as a Researcher. His research interests include autonomous underwater vehicles, unmanned aerial vehicles, and flow control.

HONG CHEN was born in Shaoxing, Zhejiang, China, in 1971. He received the Ph.D. degree in instrument science and technology from the University of Science and Technology of China, in 2006. He worked with the College of Mechatronics and Control Engineer, Shenzhen University, as a Researcher. His research interests include dynamic systems modeling and simulation and bionic robot.

SEN WANG was born in Yancheng, Jiangsu, China, in 1996. He received the B.S. degree in automation numerical control engineering from the Nanjing Institute of Technology, in 2018. Since 2019, he has been studying mechanical engineering at Shenzhen University. His research interests include autonomous underwater vehicles and embedded control.

GUOJING ZHANG was born in Maoming, Guangdong, China, in 1998. He received the B.S. degree in mechanical design, manufacturing, and automation from Shenzhen University, in 2020. He has been studying mechanical engineering at Shenzhen University, since 2020. His research interests include autonomous underwater vehicles and computational fluid dynamics.